A Grey Wolf Optimization-Based Tilt Tri-rotor UAV Altitude Control in Transition Mode

MA Yan[1], *WANG Yingxun*[1,2*], *CAI Zhihao*[1], *ZHAO Jiang*[1], *LIU Ningjun*[2]

1. School of Automation Science and Electrical Engineering, Beihang University, Beijing 100083, P. R. China;
2. Institute of Unmanned System, Beihang University, Beijing 100083, P. R. China

(Received 25 August 2021; revised 2 March 2022; accepted 13 March 2022)

Abstract: To solve the problem of altitude control of a tilt tri-rotor unmanned aerial vehicle (UAV) in the transition mode, this study presents a grey wolf optimization (GWO) based neural network adaptive control scheme for a tilt tri-rotor UAV in the transition mode. Firstly, the nonlinear model of the tilt tri-rotor UAV is established. Secondly, the tilt tri-rotor UAV altitude controller and attitude controller are designed by a neural network adaptive control method, and the GWO algorithm is adopted to optimize the parameters of the neural network and the controllers. Thirdly, two altitude control strategies are designed in the transition mode. Finally, comparative simulations are carried out to demonstrate the effectiveness and robustness of the proposed control scheme.

Key words: tilt tri-rotor unmanned aerial vehicle; altitude control; neural network adaptive control; grey wolf optimization (GWO)

CLC number: V249.122 **Document code:** A **Article ID:** 1005-1120(2022)02-0186-15

0 Introduction

Tilt rotor unmanned aerieal vehicles (UAVs) are superior to helicopters and fixed-wing aircraft in comprehensive performance, and have broad research and application prospects[1-4]. However, the aerodynamic interferences caused by tilt rotors and fixed wings are difficult to be accurately modeled. Besides, tilting rotors affect on longitudinal and horizontal forces and moments. These complex dynamic and control couples could induce angular movement interaction and have impact on flight stability. Therefore, tilt rotor UAVs are difficult to control and can hardly achieve stable flight in manual flight.

The configuration of tilt rotor UAVs changes with rotor tilting angles. If rotor tilting angles are not at 0° or 90°, the moment generated by rotor force is unparallel to x_b or z_b axis in the body coordinate frame, which causes coupled control inputs. Besides, the force generated by rotors and moments generated by aerodynamic control surfaces have uncertainties in the mode transition flight. Moreover, the relationship between control inputs and system states is strongly nonlinear. These issues affect the performance of controllers and the stability of the control system. Therefore, it is crucial to improve the effectiveness and robustness of the control system.

At present, many approaches have been proposed for tilt rotor UAVs' models and controls. Some researchers used computational fluid dynamics and theoretical calculation methods to study the interference flow field and aerodynamic interference in hover and transition modes[5-7]. In order to achieve a stable and safe mode transition process, a proportional-integral-derivative (PID) control was adopted to design the forward speed, the pitch angle and the altitude controllers[8]. A cascade PID control law was adopted to design the attitude, the altitude, and the forward flight speed controllers[9]. A deep reinforcement learning method was adopted to design position controllers and attitude controllers to achieve better trajectory tracking performance[10]. A

*Corresponding author, E-mail address: avicwyx@126.com.

How to cite this article: MA Yan, WANG Yingxun, CAI Zhihao, et al. A grey wolf optimization-based tilt tri-rotor UAV altitude control in transition mode[J]. Transactions of Nanjing University of Aeronautics and Astronautics, 2022, 39(2): 186-200.
http://dx.doi.org/10.16356/j.1005-1120.2022.02.006

predictor-based model reference adaptive control method was proposed for the lateral attitude control problem in the transition mode[11]. However, in the aforementioned control approaches, disturbances are not well considered in simulations.

Also, a reference model based robust tracking control method was designed to achieve the stability of the closed-loop system and accurate tracking of the desired command[12]. However, the controller design is based on a linear system and requires an accurate system model.

In order to enhance the performance of handling uncertain dynamics, an active disturbance rejection control (ADRC) based method was adopted to design attitude controllers with rotor tilting angles of 0°, 30°, 60°, and 90°[13-14]. A dynamic inverse based sliding mode control method was proposed for a tilt UAV attitude and position control, which is robust against disturbances[15]. These studies consider the robustness of the control system. Nonetheless, none of them considers the continuous change of the rotor tilting angle. Therefore, the control of the whole rotor tilting process is not studied.

Recently, neural network-based methods have been employed to estimate nonlinear characteristics for their good capabilities in approximation[16-18]. Specifically, the radial basis function neural network (RBFNN) is widely used for its precision and calculation speed.

Motivated by the existing related literature results, a neural network adaptive control scheme is proposed for a tilt tri-rotor UAV altitude control and attitude control. Based on the nonlinear dynamic model, continuous rotor tilting process and disturbances are all considered. To be more specific, an altitude controller and attitude controllers are designed to make the UAV track altitude command. Moreover, to address the parameter tuning problem in the control scheme, the grey wolf optimization (GWO) algorithm is used for the network parameter optimization and the controller parameter optimization. In addition, the transition process can be safer and more stable by maintaining a constant flight altitude[19], so the constant flight altitude transition is adopted. Finally, two altitude control strategies are designed to achieve a constant flight altitude in the transition process.

1 Mathematical Model

The tilt tri-rotor UAV is shown in Fig.1, and the rotor tilting process is shown in Fig.2. The kinematic definitions are shown in Fig.3. The mathematical model of the tilt tri-rotor UAV includes a rotor model and a fixed-wing model. The rotor model is established by the momentum theory and the blade element integration method. The fixed-wing model consists of the wing, the fuselage, and the tail models[20]. The UAV is light in weight and small in size. To simplify the model, the changes of the center of gravity and the moment of inertia caused by rotor tilting are ignored. The influence of rotor tilting on the force and the moment of the model is mainly considered.

The mathematical model of the tilt tri-rotor UAV is derived by using the Newton-Euler approach. The assumptions are given as follows:

(1) The tilt tri-rotor UAV is a rigid body.

Fig.1 Tilt tri-rotor UAV

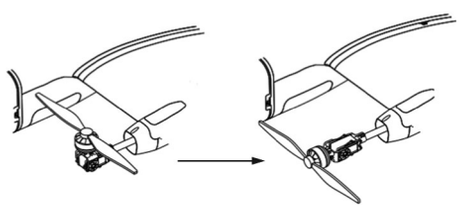

Fig.2 Rotor tilting process

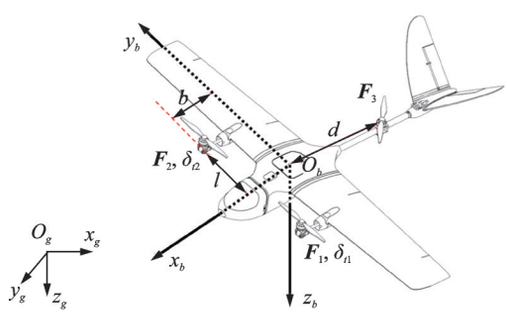

Fig.3 Tilt tri-rotor UAV kinematic definitions

(2) The tilt tri-rotor UAV is symmetrical about its longitudinal plane in the body coordinate frame.

(3) The aerodynamic interferences caused by rotors are ignored[21-22].

The coordinate frames and their definitions are given in Refs.[20-21, 23]. The hover mode is defined when the rotor tilting angle $\delta_{ti}(i=1,2)=0$, and the level flight mode is defined when $\delta_{ti}=90^\circ$. The transition mode is defined when $\delta_{ti}\in(0^\circ, 90^\circ)$. The control inputs are the motor speed $\delta_{ui}(i=1,2,3)$, the rotor tilting angle δ_{ti}, the aerodynamic control surfaces of the aileron δ_a and the v-tail $\delta_{ei}(i=1,2)$. Altitude h and Euler angles $(\boldsymbol{\phi},\boldsymbol{\theta},\boldsymbol{\psi})$ are the system outputs. The relationship of $(\ddot{\boldsymbol{\phi}},\ddot{\boldsymbol{\theta}},\ddot{\boldsymbol{\psi}})=(\dot{\boldsymbol{p}},\dot{\boldsymbol{q}},\dot{\boldsymbol{r}})$ is satisfied in the case of small Euler angles, where $(\boldsymbol{p},\boldsymbol{q},\boldsymbol{r})$ are the angular velocities. The values of inertia products are much smaller than those of the moment of inertia, so the inertia products are ignored. The attitude and altitude dynamic equations of the tilt tri-rotor UAV are given as follows[23]

$$\begin{cases}\ddot{\boldsymbol{\phi}}=\dfrac{\boldsymbol{L}}{J_{xx}}+\dfrac{J_{yy}-J_{zz}}{J_{xx}}\dot{\boldsymbol{\theta}}\dot{\boldsymbol{\psi}}\\ \ddot{\boldsymbol{\theta}}=\dfrac{\boldsymbol{M}}{J_{yy}}+\dfrac{J_{zz}-J_{xx}}{J_{yy}}\dot{\boldsymbol{\phi}}\dot{\boldsymbol{\psi}}\\ \ddot{\boldsymbol{\psi}}=\dfrac{\boldsymbol{N}}{J_{zz}}+\dfrac{J_{xx}-J_{yy}}{J_{zz}}\dot{\boldsymbol{\phi}}\dot{\boldsymbol{\theta}}\\ \ddot{z}=\dfrac{-F}{m}\cos\boldsymbol{\phi}\cos\boldsymbol{\theta}+\boldsymbol{g}\end{cases}\tag{1}$$

where $(\boldsymbol{L},\boldsymbol{M},\boldsymbol{N})$ are the control torques and (J_{xx},J_{yy},J_{zz}) the moment of inertia. F is the control thrust. According to Fig.3, the expressions of F and $(\boldsymbol{L},\boldsymbol{M},\boldsymbol{N})$ in the body coordinate frame are given as follows[20-21]

$$\begin{cases}F=F_1\cdot\cos\delta_{t1}+F_2\cdot\cos\delta_{t2}+F_3+F_{\text{aero}}\\ L=(F_1\cdot\cos\delta_{t1}+F_2\cdot\cos\delta_{t2})\cdot l+L_{\text{aero}}\\ M=(F_1\cdot\cos\delta_{t1}+F_2\cdot\cos\delta_{t2})\cdot b-F_3\cdot d+M_{\text{aero}}\\ N=(F_1\cdot\sin\delta_{t1}+F_2\cdot\sin\delta_{t2})\cdot l+N_{\text{aero}}\end{cases}\tag{2}$$

where $F_i(i=1,2,3)$ is the rotor force. l, b and d are the geometric length; and F_{aero}, L_{aero}, M_{aero}, and N_{aero} the aerodynamic force and aerodynamic moments, respectively. Rotor torques are ignored in Eq.(2).

Remark 1 Polynomials with $F_i(i=1,2,3)$ are defined as the multirotor control, and those with subscript aero are defined as the fixed-wing control.

In the level flight mode, F_3 is 0, F_1 and F_2 are pulling forces and included in the fixed-wing control. The multirotor control is adopted in the hover mode, and the fixed-wing control is adopted in the level flight mode. In transition mode, the fixed-wing control is adopted depending on the rotor tilting angle and the forward flight speed.

In Eq.(2), the rotor tilting angle $\delta_{ti}(i=1,2)$ affects F and $(\boldsymbol{L},\boldsymbol{M},\boldsymbol{N})$, which shows the unique control characteristics of the tilt rotor UAV.

2 GWO-Based RBFNN Control

RBFNN is adopted for its nonlinear function approximate ability. The neural network adaptive law is derived by the Lyapunov method, and the stability of the control system is guaranteed by adjusting the adaptive weight matrix[24]. The framework of GWO-based RBFNN control scheme is shown in Fig.4.

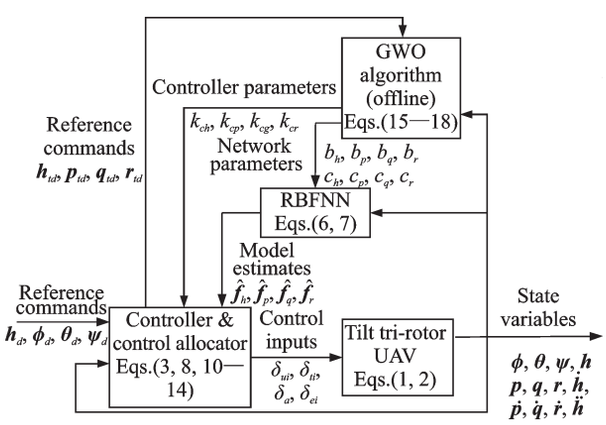

Fig.4 Tilt tri-rotor control block diagram

As presented in Fig.4, the proposed control system includes the controller and the control allocator, RBFNN, GWO, and the tilt tri-rotor UAV model. The controller and the control allocator are used to obtain desired control outputs. RBFNN is used to estimate uncertainties or disturbances of the tilt tri-rotor UAV model. GWO is used to optimize network parameters and controller parameters. The tilt tri-rotor UAV model is described by Eqs.(1,2).

2.1 RBFNN controller design

The tilt tri-rotor UAV controller design includes the attitude controller design and the altitude controller design. The attitude controllers include the angular controllers and the angular velocity controllers. The angular controllers are designed by the proportional control, and the control outputs are the desired angular velocities.

$$\begin{cases} \boldsymbol{p}_{sp} = k_{p\phi} \cdot (\boldsymbol{\phi}_{sp} - \boldsymbol{\phi}) \\ \boldsymbol{q}_{sp} = k_{p\theta} \cdot (\boldsymbol{\theta}_{sp} - \boldsymbol{\theta}) \\ \boldsymbol{r}_{sp} = k_{p\psi} \cdot (\boldsymbol{\psi}_{sp} - \boldsymbol{\psi}) \end{cases} \tag{3}$$

where $(\boldsymbol{p}_{sp}, \boldsymbol{q}_{sp}, \boldsymbol{r}_{sp})$ are the desired angular velocities, $(k_{p\phi}, k_{p\theta}, k_{p\psi})$ the adjustable controller parameters, $(\boldsymbol{\phi}_{sp}, \boldsymbol{\theta}_{sp}, \boldsymbol{\psi}_{sp})$ the desired attitude angles, and $(\boldsymbol{\phi}, \boldsymbol{\theta}, \boldsymbol{\psi})$ the actual attitude angles.

The roll angular velocity controller is designed as an example to show the process of RBFNN controller design. The roll angular velocity dynamic equation is given as follows

$$\dot{p} = \left(\boldsymbol{L} + \left(J_{yy} - J_{zz}\right)\dot{\boldsymbol{\theta}}\dot{\boldsymbol{\psi}}\right) \Big/ J_{xx} = \boldsymbol{f}_p + b_p \cdot \boldsymbol{U}_p \tag{4}$$

where $\boldsymbol{f}_p = \left(\left(J_{yy} - J_{zz}\right) \Big/ J_{xx}\right)\dot{\boldsymbol{\theta}}\dot{\boldsymbol{\psi}}$, $b_p = 1/J_{xx}$, $\boldsymbol{U}_p = \boldsymbol{L}$. The desired roll angular velocity command is defined as $\boldsymbol{y}_d = \boldsymbol{p}_{sp}$. The tracking error of the roll angular velocity command is defined as $\boldsymbol{e}_p = \boldsymbol{y}_d - \boldsymbol{p}$, and $\boldsymbol{E}_p = \left(\boldsymbol{e}_p, \dot{\boldsymbol{e}}_p\right)^{\mathrm{T}}$. The roll angular velocity control law is designed as follows

$$\boldsymbol{U}_p = \frac{1}{b_p}\left[-\boldsymbol{f}_p + \boldsymbol{K}_p \cdot \boldsymbol{E}_p\right] \tag{5}$$

where $\boldsymbol{K}_p = (k_{pp}, k_{dp})$ is the controller parameter.

RBFNN is used to estimate $\boldsymbol{f}_p$ and other disturbances[24]. In this section, RBFNN is introduced as follows

$$h_j = g\left(\left\| \boldsymbol{x} - \boldsymbol{c}_j \right\|^2 \Big/ b_j^2\right) \tag{6}$$

$$\hat{\boldsymbol{f}} = \boldsymbol{W}^{\mathrm{T}} \cdot \boldsymbol{H}(\boldsymbol{x}) + \varepsilon \tag{7}$$

where $\boldsymbol{x}$ is the network input vector, j the node number of the hidden layer, $\boldsymbol{W}$ the weight matrix, ε the approximated error, $\hat{\boldsymbol{W}}_p^{\mathrm{T}}$ the estimated value of the ideal weight matrix $\boldsymbol{W}_p^{\mathrm{T}}$. $\boldsymbol{H} = \left[h_1, h_2, \cdots, h_n\right]^{\mathrm{T}}$ is the output vector of Gaussian function. In Eqs.(6, 7), the input is $\boldsymbol{x}_p = \left(\boldsymbol{e}_p, \dot{\boldsymbol{e}}_p\right)^{\mathrm{T}}$, and the output is $\hat{\boldsymbol{f}}_p = \hat{\boldsymbol{W}}_p^{\mathrm{T}} \cdot \boldsymbol{H}_p(x)$.

To reduce the number of adjustable parameters, $b_j = b$ and $\boldsymbol{c}_j = c \times \begin{bmatrix} -j, -j+1, \cdots, 0, \cdots, j-1, j \\ -j, -j+1, \cdots, 0, \cdots, j-1, j \end{bmatrix}$ are defined, where b and c are adjustable network parameters.

Using $\hat{\boldsymbol{f}}_p$ instead of $\boldsymbol{f}_p$, we have

$$\begin{cases} \boldsymbol{U}_p = \dfrac{1}{b_p}\left[-\hat{\boldsymbol{f}}_p + \boldsymbol{K}_p \cdot \boldsymbol{E}_p\right] \\ \hat{\boldsymbol{f}}_p = \hat{\boldsymbol{W}}_p^{\mathrm{T}} \cdot \boldsymbol{H}_p(\boldsymbol{x}) \end{cases} \tag{8}$$

The adaptive law of the weight matrix is

$$\dot{\hat{\boldsymbol{W}}}_p = -\gamma \cdot \boldsymbol{E}_p^{\mathrm{T}} \cdot \boldsymbol{P} \cdot \boldsymbol{B} \cdot \boldsymbol{H}_p(\boldsymbol{x}) \tag{9}$$

The definitions of parameters in Eq.(9) and the stability proof of the control law (8) are given in Ref.[24].

Using the same process as the roll angular velocity controller design, the pitch angular velocity controller, the yaw angular velocity controller, and the altitude controller are obtained as follows

$$\begin{cases} \boldsymbol{U}_q = \dfrac{1}{b_q}\left[-\hat{\boldsymbol{f}}_q + \boldsymbol{K}_q \cdot \boldsymbol{E}_q\right] \\ \hat{\boldsymbol{f}}_q = \hat{\boldsymbol{W}}_q^{\mathrm{T}} \cdot \boldsymbol{H}_q(\boldsymbol{x}) \end{cases} \tag{10}$$

$$\begin{cases} \boldsymbol{U}_r = \dfrac{1}{b_r}\left[-\hat{\boldsymbol{f}}_r + \boldsymbol{K}_r \cdot \boldsymbol{E}_r\right] \\ \hat{\boldsymbol{f}}_r = \hat{\boldsymbol{W}}_r^{\mathrm{T}} \cdot \boldsymbol{H}_r(\boldsymbol{x}) \end{cases} \tag{11}$$

$$\begin{cases} \boldsymbol{U}_h = \dfrac{1}{b_h}\left[-\hat{\boldsymbol{f}}_h + \ddot{\boldsymbol{h}}_d + \boldsymbol{K}_h \cdot \boldsymbol{E}_h\right] \\ \hat{\boldsymbol{f}}_h = \hat{\boldsymbol{W}}_h^{\mathrm{T}} \cdot \boldsymbol{H}_h(\boldsymbol{x}) \end{cases} \tag{12}$$

where $(b_q, b_r, \boldsymbol{b}_h) = (1/J_{yy}, 1/J_{zz}, -\cos\boldsymbol{\phi}\cos\boldsymbol{\theta}/m)$. $\hat{\boldsymbol{f}}_q$, $\hat{\boldsymbol{f}}_r$, and $\hat{\boldsymbol{f}}_h$ are the estimates of $\boldsymbol{f}_q = \left(\left(J_{zz} - J_{xx}\right)/J_{yy}\right)\dot{\boldsymbol{\phi}}\dot{\boldsymbol{\psi}}$, $\boldsymbol{f}_r = \left(\left(J_{xx} - J_{yy}\right)/J_{zz}\right)\dot{\boldsymbol{\phi}}\dot{\boldsymbol{\theta}}$, and $\boldsymbol{f}_h = \boldsymbol{g}$, respectively. $\boldsymbol{K}_q = \left(k_{pq}, k_{dq}\right)$, $\boldsymbol{K}_r = \left(k_{pr}, k_{dr}\right)$, and $\boldsymbol{K}_h = \left(k_{ph}, k_{dh}\right)$ are the controller parameters. $\boldsymbol{E}_q = \left(\boldsymbol{e}_q, \dot{\boldsymbol{e}}_q\right)^{\mathrm{T}}$ is the pitch angular velocity command tracking error and its derivative, $\boldsymbol{E}_r = \left(\boldsymbol{e}_r, \dot{\boldsymbol{e}}_r\right)^{\mathrm{T}}$ the yaw angular velocity command tracking error and its derivative, $\boldsymbol{E}_h = \left(\boldsymbol{e}_h, \dot{\boldsymbol{e}}_h\right)^{\mathrm{T}}$ the altitude command tracking error and its derivative, and $\ddot{\boldsymbol{h}}_d$ the second-order derivative of the desired altitude command.

In the level flight mode, the pitch angle is used

for the altitude control. The desired pitch angle command is generated by the PID controller, which is given as follows

$$\theta_{sp}=\bar{k}_{p\theta}\cdot e_h+k_{i\theta}\cdot\int e_h\,\mathrm{d}t+k_{d\theta}\cdot\dot{e}_h \tag{13}$$

where $\bar{k}_{p\theta}$, $k_{i\theta}$, and $k_{d\theta}$ are the controller parameters.

The tracking differentiator (TD) is used to generate transition signals of the command signal. TD is given as follows

$$\mathrm{TD}=\omega_n^2/\left(s^2+2\xi\omega_n s+\omega_n^2\right) \tag{14}$$

where ξ and ω_n are the adjustable parameters. By adjusting the values of ξ and ω_n, the expected transition signal of the command signal and the first-order and second-order derivative signals of the transition signal are obtained. The overshoot of the transition signal relative to the command signal becomes smaller as ξ increases, and the transition signal tracks the command signal faster as ω_n increases.

Remark 2 For the position control, the range of ξ is [0.8, 1], and the range of ω_n is [0.5, 5]. For angular velocity control, the range of ξ is [0.8, 1], and the range of ω_n is [20, 40]. The specific values of ξ and ω_n are determined according to physical actuator limitations and the desired control performance.

2.2 GWO algorithm

GWO was proposed by Mirjalili et al.[25] After being tested with 29 mathematical optimization problems and three structural design problems, GWO was found very competitive compared with particle swarm optimization (PSO), the gravitational search algorithm (GSA), and the evolution strategy (ES). GWO has been successfully applied to parameter optimization[26-27]. In regard of this, GWO is adopted to optimize adjustable parameters in the proposed control scheme. In this section, GWO is introduced as follows

$$\begin{cases}\boldsymbol{D}_\alpha=\left|\boldsymbol{C}_1\cdot\boldsymbol{X}_\alpha-\boldsymbol{X}\right|\\ \boldsymbol{D}_\beta=\left|\boldsymbol{C}_2\cdot\boldsymbol{X}_\beta-\boldsymbol{X}\right|\\ \boldsymbol{D}_\delta=\left|\boldsymbol{C}_3\cdot\boldsymbol{X}_\delta-\boldsymbol{X}\right|\end{cases} \tag{15}$$

$$\boldsymbol{A}=2\boldsymbol{a}\cdot\boldsymbol{r}_1-\boldsymbol{a},\quad \boldsymbol{C}=2\cdot\boldsymbol{r}_2 \tag{16}$$

$$\begin{cases}\boldsymbol{X}_1=\boldsymbol{X}_\alpha-\boldsymbol{A}_1\cdot\left(\boldsymbol{D}_\alpha\right)\\ \boldsymbol{X}_2=\boldsymbol{X}_\beta-\boldsymbol{A}_2\cdot\left(\boldsymbol{D}_\beta\right)\\ \boldsymbol{X}_3=\boldsymbol{X}_\delta-\boldsymbol{A}_3\cdot\left(\boldsymbol{D}_\delta\right)\end{cases} \tag{17}$$

$$\boldsymbol{X}(t+1)=(\boldsymbol{X}_1+\boldsymbol{X}_2+\boldsymbol{X}_3)/3 \tag{18}$$

where α, β, and δ are the current best individual, the current suboptimal individual, and the current third best individual in GWO algorithm, respectively. $\boldsymbol{A}_i(i=1,2,3)$ and $\boldsymbol{C}_i(i=1,2,3)$ are the parameters. $\boldsymbol{a}$ linearly decreases from 2 to 0. $\boldsymbol{r}_1$ and $\boldsymbol{r}_2$ are the random vectors in [0, 1]. $\boldsymbol{X}$, $\boldsymbol{X}_1$, $\boldsymbol{X}_2$, and $\boldsymbol{X}_3$ are the position vectors of current search agents, α, β, and δ, respectively. The implementation procedure of GWO is shown in Fig.5.

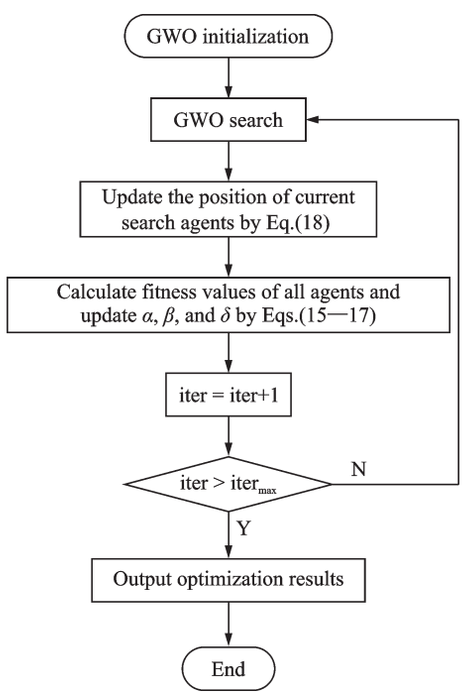

Fig.5 Implementation procedure of GWO

In Fig.5, iter is the current iteration and $\mathrm{iter}_{\max}$ the maximum iteration number. The pseudo code of GWO is presented as follows:

Begin

Step 1 Initialize the wolf population. In detail, initialize the population size N_p, the maximum iteration number $\mathrm{iter}_{\max}$, the spatial dimension D, the boundaries and the initial positions of the grey wolves. Initialize parameters of $\boldsymbol{a}$, $\boldsymbol{A}$, and $\boldsymbol{C}$.

Step 2 Calculate the fitness values of each grey wolf, and find α, β, and δ.

Step 3 For each grey wolf, if the grey wolf goes beyond the search space, return it back. Update the position of each current grey wolf by Eq.(18).

Step 4 Calculate the fitness values of all grey wolves and update the positions of α, β, and δ by Eqs.(15—17).

Step 5 Output the best grey wolf when iteration number reaches its max value. Otherwise, go to step 3.

End.

The complexity of GWO is analyzed. In detail, at Step 1, initializing N_p gray wolf individuals in D-dimensional search space requires $N_p \times D$ computations. At Step 2, calculating the fitness values of each grey wolf requires N_p computations, and the complexity of the fitness value calculation is $O(D)$. The number of computations is $3 \times N_p - 3$ for calculating $\boldsymbol{X}_\alpha$, $\boldsymbol{X}_\beta$, and $\boldsymbol{X}_\gamma$, and the number of computations is 1 for recording $\boldsymbol{X}_\alpha$. At Step 3, calculating distances among other grey wolves and $\boldsymbol{X}_\alpha$, $\boldsymbol{X}_\beta$, and $\boldsymbol{X}_\gamma$ requires $3 \times N_p - 3$ computations, and updating positions of $\boldsymbol{X}_\alpha$, $\boldsymbol{X}_\beta$, and $\boldsymbol{X}_\gamma$ with prey requires $3D+1$ computations[28]. At Step 4, the number of computations is a constant for updating the parameters of $\boldsymbol{a}$, $\boldsymbol{A}$, and $\boldsymbol{C}$. Among these computations, $O(D)$ is the biggest and much larger than the others. The maximum iteration number is $\text{iter}_{\max}$. By approximating the calculation, the time complexity of the GWO algorithm is about $O(D \times \text{iter}_{\max})$.

To reduce the number of adjustable parameters, parameter k_c is introduced, which satisfied $k_d = 2k_c$, and $k_p = k_c^2$ in Eq.(6). Together with network parameters b and c, each controller has three adjustable parameters. The parameters of the angular velocity controllers are obtained, and then the parameters of the altitude controller are obtained. The cost functions are designed as follows

$$f_{\text{attcost}} = \int \left(|\boldsymbol{p} - \boldsymbol{p}_{td}| + |\boldsymbol{q} - \boldsymbol{q}_{td}| + |\boldsymbol{r} - \boldsymbol{r}_{td}| \right) \mathrm{d}t \quad (19)$$

$$f_{\text{hcost}} = \int (|\boldsymbol{h} - \boldsymbol{h}_{td}|) \mathrm{d}t \quad (20)$$

where f_{attcost} and f_{hcost} are the cost functions of the angular velocity controllers and the altitude controller, respectively. $(\boldsymbol{p}, \boldsymbol{q}, \boldsymbol{r})$ and $\boldsymbol{h}$ are the actual signals, and $(\boldsymbol{p}_{td}, \boldsymbol{q}_{td}, \boldsymbol{r}_{td})$ and $\boldsymbol{h}_{td}$ the reference commands.

Remark 3 The numerical relationships of k_d, k_c, and k_p are explained as follows. By substituting the control law $\boldsymbol{U}_h$ (Eq.(12)) into $\ddot{\boldsymbol{z}}$ (Eq.(1)), we have error equations $\ddot{\boldsymbol{e}}_h + k_{dh} \cdot \dot{\boldsymbol{e}}_h + k_{ph} \cdot \boldsymbol{e}_h = \boldsymbol{\varepsilon}_h$, and $\boldsymbol{\varepsilon}_h = \hat{\boldsymbol{f}}_h - \boldsymbol{f}_h$. By adopting the adaptive law of the weight matrix, $\boldsymbol{\varepsilon}_h$ decreases and approaches to 0. By adopting the relationship of k_{ph} and k_{dh}, the Laplace transformation of error equation is $s^2 + 2k_{ch} \cdot s + k_{ck}^2 = 0$. If $k_{ch} > 0$, we have $s < 0$. For the angular velocity controllers (Eqs.(8, 10—11)), the Laplace transformation of error equations are $k_{dp} \cdot s + k_{pp} = 0$, $k_{dq} \cdot s + k_{pq} = 0$, and $k_{dr} \cdot s + k_{pr} = 0$. If $k_{cp} > 0$, $k_{cq} > 0$, and $k_{cr} > 0$, we have $k_{dp} > 0$, $k_{pp} > 0$, $k_{dq} > 0$, $k_{pq} > 0$, $k_{dr} > 0$, and $k_{pr} > 0$. And the stability of the control system is guaranteed.

Remark 4 The neural network in this paper is used online, and the computational burden must be considered. The computational speed of the method is correlated with the processor speed and storage capacity. The faster on-board processor with more memory space could be demanded in actual flight. Based on the computation speed on the computer, we recommend that the processor's operating frequency is at least 1 GHz (such as DJI Manifold 2-C), and this value needs to be tested in actual scenarios.

2.3 Control allocation and altitude control strategy

The control effectiveness of aerodynamic control surfaces is positively correlated to the forward flight speed. Therefore, the control allocation authority is set as a function of the forward flight speed. When the forward flight speed is lower than v_0, the UAV is controlled by the multirotor control. When the forward flight speed reaches v_1, the fixed-wing control is completely adopted. When the forward flight speed is between v_0 and v_1, a linear allocation method is adopted, which is given as follows

$$k_{\text{multirotor}} = \begin{cases} 1 & v < v_0 \\ (v_1 - v) / (v_1 - v_0) & v_0 \leqslant v \leqslant v_1 \\ 0 & v > v_1 \end{cases} \quad (21)$$

$$k_{\text{fixed-wing}} = 1 - k_{\text{multirotor}} \quad (22)$$

where $k_{\text{multirotor}}$ and $k_{\text{fixed-wing}}$ are the weights of the multirotor control and the fixed-wing control, respectively.

Two altitude control strategies are proposed for the altitude control in the transition mode, hereinafter referred to as strategy Ⅰ and strategy Ⅱ, respectively. Strategy Ⅰ is to give the UAV a forward speed which is greater than v_1. The aerodynamic control surfaces have control effectiveness before mode transition, and the fixed-wing control is adopted in the mode transition flight.

Strategy Ⅱ is based on the value of the rotor tilting angle $\delta_{ti}(i=1,2)$. The multirotor control is adopted before $\delta_{ti}(i=1,2)$ reaches a user set value δ_{tilt0}, and the fixed-wing control is adopted when $\delta_{ti}(i=1,2)\geqslant\delta_{\text{tilt0}}$. It is found that δ_{tilt0} can be selected in the range of 40°— 60°, and within this range different values of δ_{tilt0} will not show great impact on the transition mode flight.

3 Numerical Simulations

In this section, comparative simulations are carried out to test the performance of the proposed control scheme. The effectiveness of the proposed method is verified through comparison between the proposed method, the ADRC and the PID methods. Environmental disturbances, measurement errors, and motor model errors are considered to verify the robustness of the proposed method.

Considering the former research results[21], the simulation accuracies in this paper are set as follows. The maximum altitude tracking error is less than 1 m, and the steady-state altitude tracking error is less than 0.1 m. The maximum attitude angle tracking error is less than 12°, and the steady-state attitude tracking error is less than 2°.

Environmental disturbances, measurement errors, and motor model errors are collectively named as disturbances. The environmental disturbances are modeled as the external force and the external moments. The external force $\boldsymbol{F}_{\text{dis}}$ is modeled as a constant, and the external moments $(\boldsymbol{L}_{\text{dis}},\boldsymbol{M}_{\text{dis}},\boldsymbol{N}_{\text{dis}})$ are modeled as a constant, a sinusoidal, and the square wave. The disturbances mentioned above are given as follows

$$\begin{cases}\boldsymbol{F}_{\text{dis}}=-2\\ \boldsymbol{L}_{\text{dis}}=0.3\\ \boldsymbol{M}_{\text{dis}}=0.3+0.1\cdot\sin(4\pi t)\\ \boldsymbol{N}_{\text{dis}}=0.4\cdot\text{sign}\big(\sin(4\pi t)\big)\end{cases}\tag{23}$$

The measurement errors are divided into the altitude measurement error and the attitude measurement error. These errors are given as follows

$$\begin{cases}m_h=m_h+0.2+0.1\cdot(\text{rand}-0.5)\\ m_\phi=m_\phi+0.1\cdot|m_\phi|\cdot\text{rand}\\ m_\theta=m_\theta+0.1\cdot|m_\theta|\cdot\text{rand}\\ m_\psi=m_\psi+0.1\cdot|m_\psi|\cdot\text{rand}\end{cases}\tag{24}$$

where m_h is the altitude measurement value, m_ϕ the ϕ measurement value, m_θ the θ meausrement value, and m_ψ the ψ measurement value.

The brushless direct current motor is modeled as a first-order inertial system, which is given as follows

$$G(\text{s})=1/(Ts+1)\tag{25}$$

where T is the time constant and increased by 20% as the motor model error.

3.1 Hover mode simulation results

Table 1 presents the parameters of the tilt trirotor UAV in Fig.1.

Table 1 UAV parameters

Variable	Description	Value
m/ kg	Mass	4
l/ m	Geometric length	0.32
b/m	Geometric length	0.26
d/m	Geometric length	0.44
J_{xx}/ (kg•m^{-2})	Moment of inertia	0.426 3
J_{yy}/ (kg•m^{-2})	Moment of inertia	0.448 2
J_{zz}/ (kg•m^{-2})	Moment of inertia	0.648 0

The desired altitude command is set to $h_{sp}=10$ m, and the desired attitude angle commands are set to $\phi_{sp}=\theta_{sp}=\psi_{sp}=0$. The initial position, velocities, attitude angles, and angular velocities are all set to 0. $(k_{p\phi},k_{p\theta},k_{p\psi})=(2,2,2)$. The parameters of TD are set to $\xi_h=1$, $\omega_{nh}=0.8$, $\xi_\phi=\xi_\theta=\xi_\psi=1$, and $\omega_{n\phi}=\omega_{n\theta}=\omega_{n\psi}=40$. The transi-

tion signals of altitude command are shown in Fig.6.

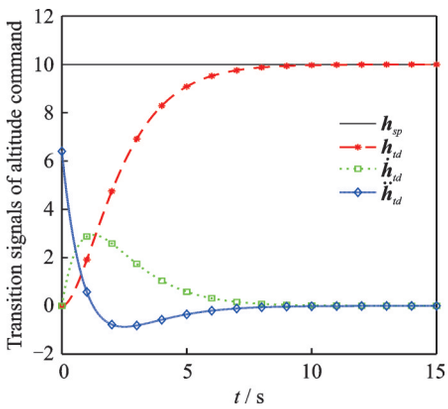

Fig.6 Transition signals of altitude command

In Fig.6, the black line is the desired altitude command h_{sp}. The red line is the transition signal of h_{sp}, and is named as h_{td}. The green line is $\dot{h}_{td}$, and the blue line is $\ddot{h}_{td}$. By using TD, a smooth transition command signal and its first-order and second-order derivative signals are obtained.

The structure of ADRC is given in Ref.[29], and the structure of PID is given in Ref.[9]. The simulation parameters of ADRC are $w_{oh}=3$, $w_{op}=3$, $w_{oq}=6$, $w_{or}=5$, $w_{ch}=80$, $w_{cp}=3$, $w_{cq}=4$, and $w_{cr}=4$. The simulation parameters of PID are $k_{p\_h}=3$, $k_{p\_vh}=3$, $k_{i\_vh}=0.075$, $k_{d\_vh}=0.01$, $k_{p\_p}=5$, $k_{p\_q}=8$, and $k_{p\_r}=6.5$.

Fig.7 shows the stable altitude control results by different control methods. The convergence speed of PID control is relatively slower than those of that of the other two methods. In Fig.8, the proposed control method under disturbances has the altitude tracking error less than 0.2 m (2% error band) within 1.36 s, which is less than those of

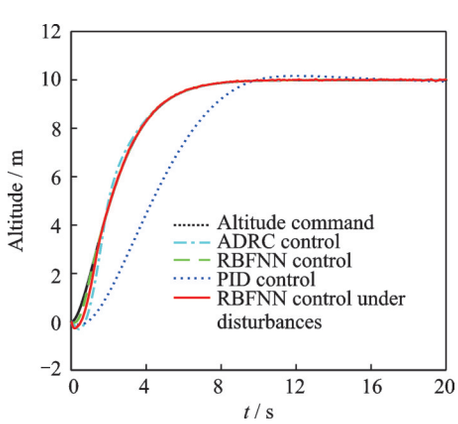

Fig.7 Altitude transition command control results

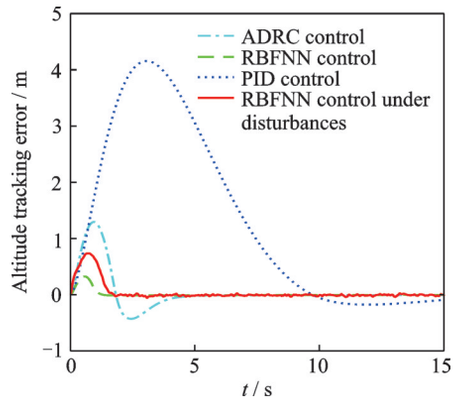

Fig.8 Altitude transition command tracking errors

ADRC (about 3.39 s) and PID control (about 9.04 s). The maximum altitude tracking error is about 0.74 m, which is less than those of ADRC (about 1.29 m) and PID control (about 4.16 m).

Figs.9—11 show that the attitude control results of the proposed control method are better than those of ADRC and PID control. The maximum angle tracking error (about 11.47°, pitch angle) and the steady-state tracking error (about 1.52°, yaw angle) are within the simulation control accuracies.

Integral of absolute value of error criterion

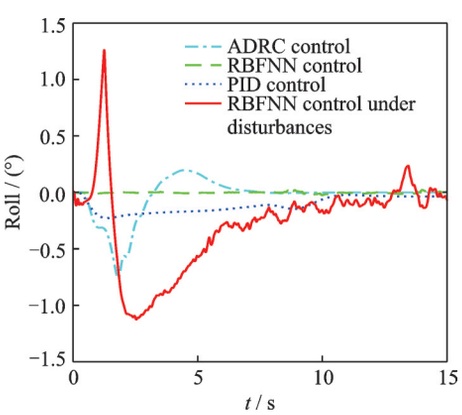

Fig.9 Roll angle control results

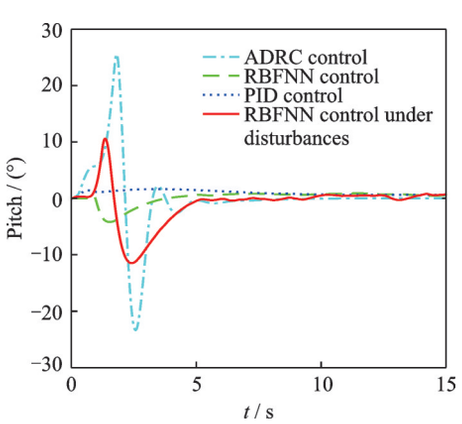

Fig.10 Pitch angle control results

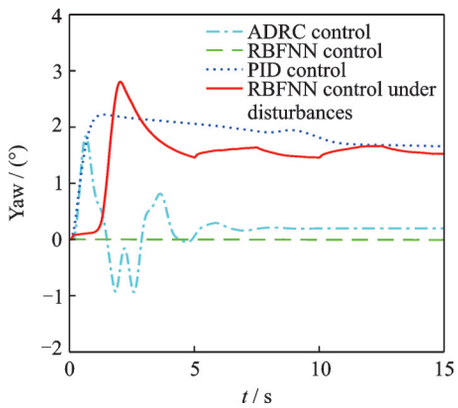

Fig.11 Yaw angle control results

(IAE) values of ADRC, RBFNN and PID control are shown in Table 2.

Table 2 IAE values in hover mode

Method	Altitude	Roll	Pitch	Yaw
ADRC	2.185 6	1.342 7	37.755 4	5.638 7
RBFNN	0.302 7	0.083 7	13.308 2	0.048 9
PID	21.759 0	1.818 2	18.515 5	36.145 6
RBFNN (disturbances)	0.940 1	5.478 5	30.179 5	31.501 9

Table 2 is the IAE values of different control methods. It can be seen that RBFNN has the smallest IAE value. The UAV is under disturbances, and RBFNN still has acceptable control performance.

Fig. 12 is the fitness value results of GWO, PSO, and the genetic algorithm (GA). It can be seen that GWO has the highest convergence precision compared with PSO and GA. GWO fitness value converges to about 3.56×10^{-4} after about 30 iterations. Fig.13 shows the fitness value in the altitude control by GWO. Tables 3—4 present parameter optimization results of the angular velocity controllers and the altitude controller by GWO.

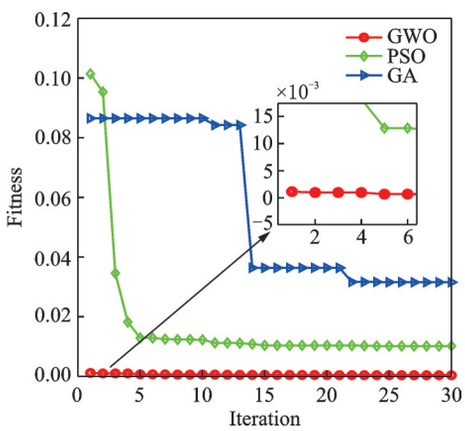

Fig.12 Fitness value in angular velocity control

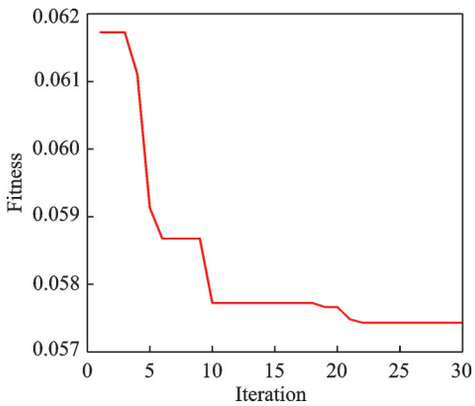

Fig.13 Fitness value in altitude control

Table 3 Optimization results of angular velocity controller parameters

Parameter	Value	Range
k_{cp}	6.424 4	[1,10]
b_p	4.871 6	[0.5,5]
c_p	0.210 2	[0.1,1]
k_{cq}	1.438 7	[1,10]
b_q	1.274 2	[0.5,5]
c_q	0.194 0	[0.1,1]
k_{cr}	1	[1,10]
b_r	0.56	[0.5,5]
c_r	0.278 6	[0.1,1]

Table 4 Optimization results of altitude controller parameters

Parameter	Value	Range
k_{ch}	10	[1,10]
b_h	0.5	[0.5,5]
c_h	0.11	[0.1,1]

Figs.7—11 show that the proposed method has better altitude and attitude control results. The altitude and attitude controller parameters in Tables 3—4 are used in transition mode simulations.

3.2 Transition mode simulation results

3.2.1 Altitude control of Strategy Ⅰ

In Strategy Ⅰ, the initial forward flight speed is set to 15 m/s. The initial altitude and altitude commands are all set to 30 m. The initial position, attitude angles, and angular velocities of the UAV are all set to 0. The rotor tilting angles change uniformly from 5 s to 30 s. Defining the process of increasing the rotor tilting angle from 0° to 90° is the positive transition, and the process of decreasing the rotor tilting angle from 90° to 0° is the reverse transition.

Simulation results of the positive transition are shown in Figs. 14—17. Fig. 14 shows the change of the rotor tilting angle in the positive transition. In Fig. 15, the maximum altitude tracking error of the proposed method is about 0.24 m, which is less than PID control (about 0.52 m), and that of PID control also has a steady-state error of about 0.3 m. The altitude tracking error in Fig. 15 is smaller than that in Ref. [30] (about 7 m) and that in Ref. [31] (about 1 m). IAE values of PID, RBFNN, and

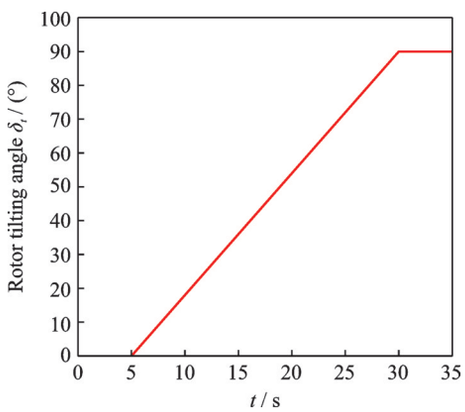

Fig. 14 Rotor tilting angle in positive transition

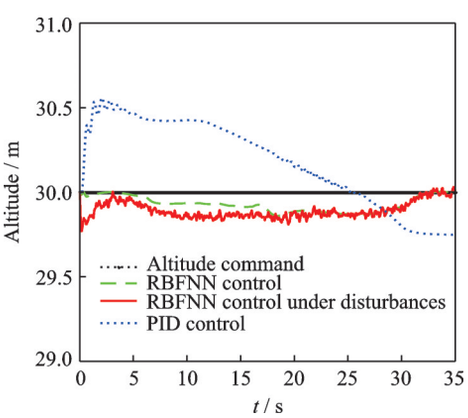

Fig. 15 Altitude results in positive transition of Strategy Ⅰ

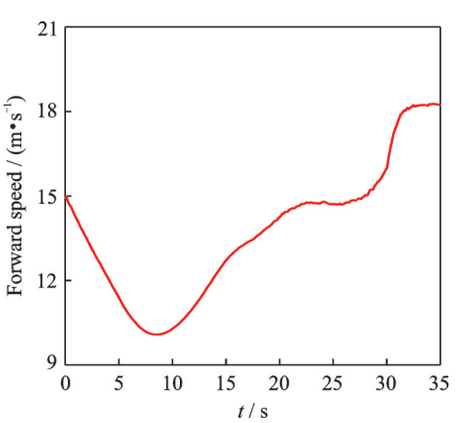

Fig. 16 Forward speed result by RBFNN under disturbances in positive transition of Strategy Ⅰ

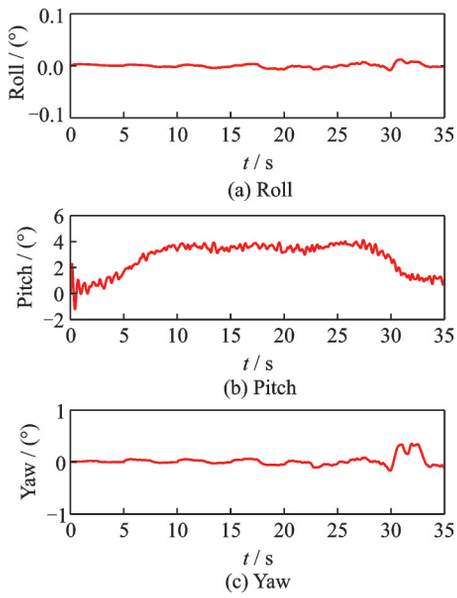

Fig. 17 Attitude results by RBFNN under disturbances in positive transition of Strategy Ⅰ

RBFNN control under disturbances are 9.532, 2.483, and 3.803 6, respectively, which shows RBFNN has better control performance.

Fig. 16 shows the forward flight speed of the UAV. The forward flight speed increases as the rotor tilting angle increases, and converges to about 18.2 m/s. In Fig. 17, the pitch angle is used for the altitude control, and its range is about [−2°, 4°]. The values of roll angle and yaw angle are both within [−1°, 1°], which shows the stable attitude control results.

Simulation results of the reverse transition are shown in Figs. 18—21. Fig. 18 shows the change of the rotor tilting angle in reverse transition. The rotor tilting angle is uniformly changed from 90° to 0°, and the angular changing rate is within the allowable

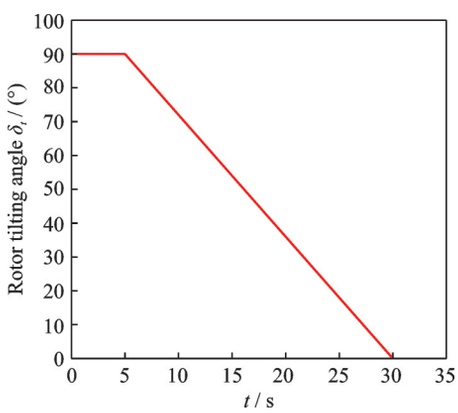

Fig. 18 Rotor tilting angle in reverse transition

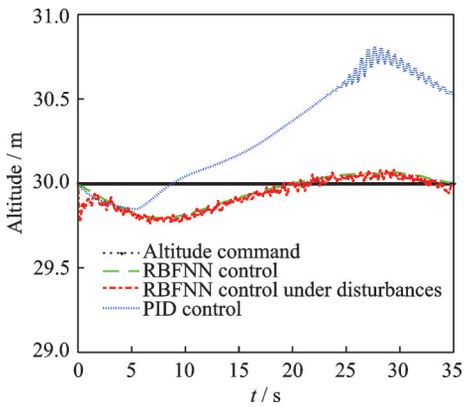

Fig.19 Altitude results in reverse transition of Strategy Ⅰ

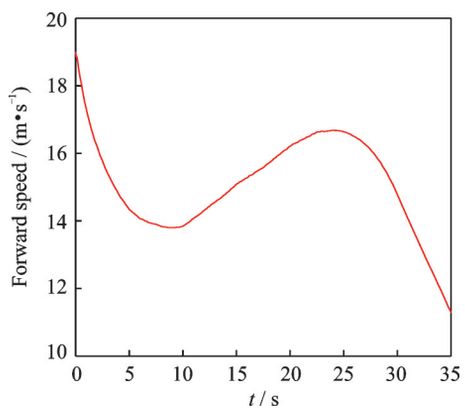

Fig.20 Forward speed result by RBFNN under disturbances in reverse transition of Strategy Ⅰ

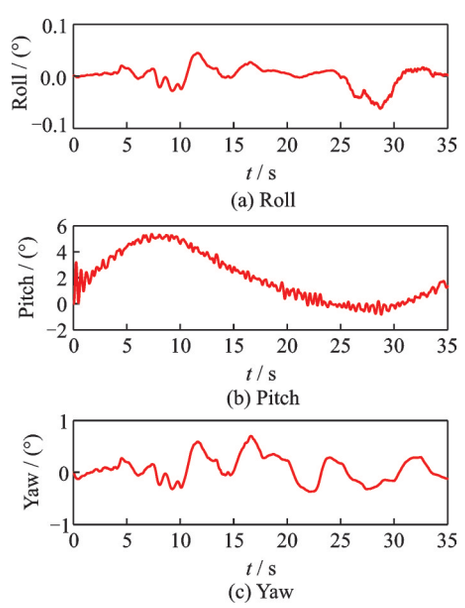

Fig.21 Attitude results by RBFNN under disturbances in reverse transition of Strategy Ⅰ

range of the UAV. Fig.19 shows the comparative results of the proposed control method and PID control. The maximum altitude tracking error of the proposed method is about 0.2 m, which is less than that of the PID control (about 0.7 m). IAE values of PID, RBFNN, and RBFNN control under disturbances are 11.758 8, 2.910 1, and 3.179 7, respectively, which shows RBFNN has better control performance.

Fig.20 shows the forward flight speed of the UAV. The forward flight speed has a negative interrelation to pitch angle. In Fig.21, the pitch angle is used for altitude control and its range is about [0°, 6°]. The values of roll angle and yaw angle are relatively small and both within [−1°, 1°], which shows the stable attitude control results.

3.2.2 Altitude control of Strategy Ⅱ

In Strategy Ⅱ, rotor tilting angle $\delta_{\text{tilt0}}=45°$ is selected as the multirotor control and the fixed-wing control switching angle. The multirotor control is adopted when $\delta_{\text{tilt0}}<45°$ and the fixed-wing control is adopted when $\delta_{\text{tilt0}}\geqslant 45°$. The initial forward flight speed is set to 0 in the positive transition simulation, and it is set to 19 m/s in the reverse transition simulation. Other initial conditions are the same as those in Strategy Ⅰ.

The change of the rotor tilting angle in the positive transition is shown in Fig.14. Simulation results of the positive transition are shown in Figs. 22—24. Fig.22 shows the comparative altitude control results of the proposed method and PID control. The maximum altitude tracking error of the proposed method is about 0.2 m, and that of PID control is about 0.6 m. PID control has a steady-state error about 0.3 m. IAE values of PID, RBFNN, and RBFNN control under disturbances are 7.558 2, 1.767 8, and 2.490 8, respectively, which shows RBFNN has better control performance.

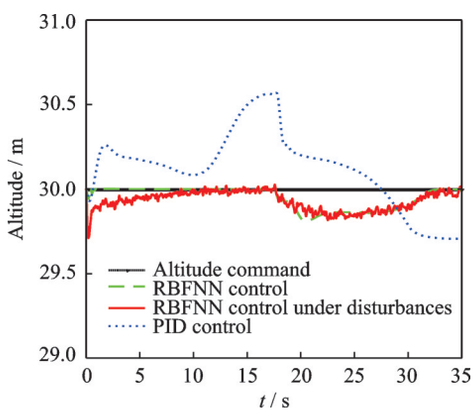

Fig.22 Altitude results in positive transition of Strategy Ⅱ

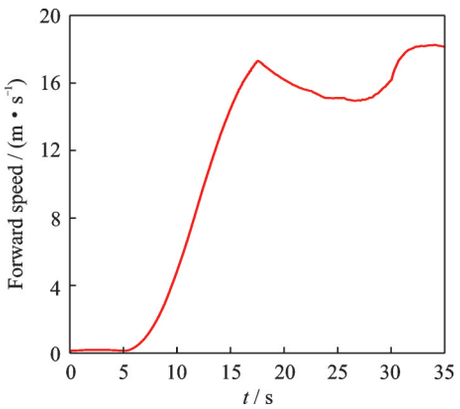

Fig.23 Forward speed result by RBFNN under disturbances in positive transition of Strategy Ⅱ

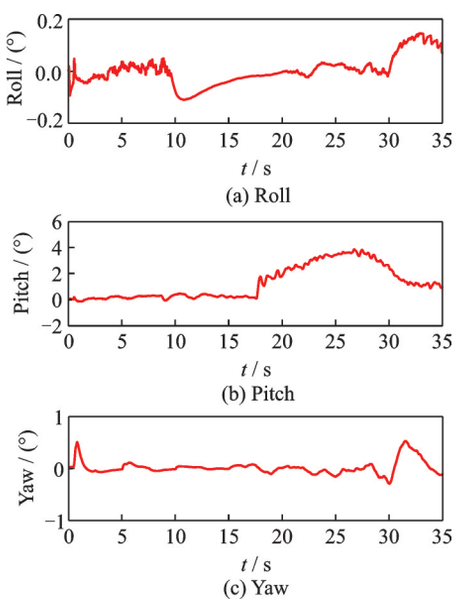

Fig.24 Attitude results by RBFNN under disturbances in positive transition of Strategy Ⅱ

In Fig.23, the forward flight speed increases as the rotor tilting angle increases, and has a negative interrelation to the pitch angle when $\delta_{\text{tilt}} \geqslant 45^\circ$, and converges to about 18.2 m/s in the fixed-wing mode. Fig.24 shows the attitude results. When $\delta_{\text{tilt}} \geqslant 45^\circ$, the pitch angle is used for the altitude control, and converges to about 1° in the fixed-wing mode. The range of the pitch angle is about [0°, 4°]. The values of the roll angle and the yaw angle are relatively small and both within [−1°, 1°], which shows the stable attitude control results.

The change of the rotor tilting angle in the reverse transition is shown in Fig.18. Simulation results of the reverse transition are shown in Figs.25—27. Fig. 25 shows the comparative altitude control

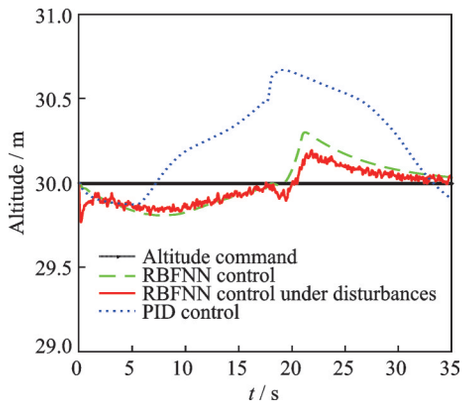

Fig.25 Altitude results in reverse transition of Strategy Ⅱ

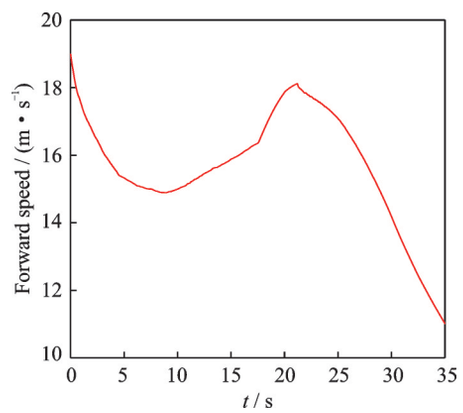

Fig.26 Forward speed result by RBFNN under disturbances in reverse transition of Strategy Ⅱ

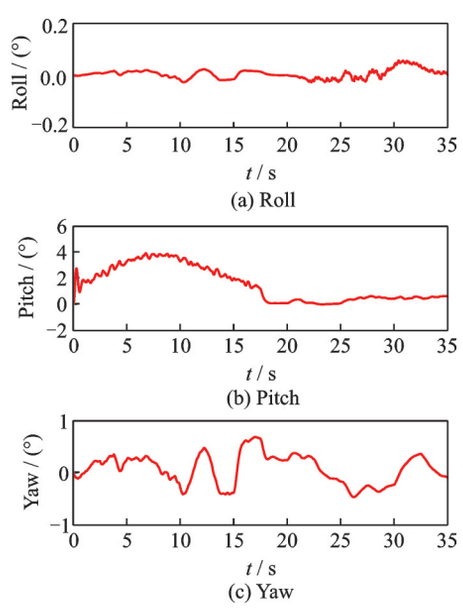

Fig.27 Attitude results by RBFNN under disturbances in reverse transition of Strategy Ⅱ

results of the proposed method and PID control. When $\delta_{\text{tilt}} \geqslant 45^\circ$, the altitude is controlled by pitch angle. After control switch, the altitude is controlled by the multirotor control. The altitude out-

puts are fluctuated due to control switch. Even under disturbances, the maximum altitude tracking error of the proposed method is about 0.26 m, which is less than that of PID control (about 0.7 m), and PID control has a steady-state error of about 0.1 m. IAE values of PID, RBFNN, and RBFNN control under disturbances are 10.540 3, 4.155 2, and 3.146 4, respectively, which shows RBFNN has better control performance.

Fig.26 shows the forward flight speed of the UAV. The forward speed has a negative interrelation to pitch angle (Fig.27) and decreases after control switch. Fig.27 shows the attitude results. When $\delta_{\text{tilt}} \geqslant 45^\circ$, the pitch angle is used for the altitude control, and converges to about 0.5° after control switch. The range of the pitch angle is about [0°, 4°]. The values of the roll angle and the yaw angle are both within [−1°, 1°], which shows the stable attitude control results.

3.3 Comparison of altitude control strategies

Strategy Ⅰ needs an initial forward flight speed. The aerodynamic control surfaces have control effectiveness before transition mode starts, and only the fixed-wing control is adopted. Strategy Ⅰ can achieve smoother altitude and forward flight speed results in the transition mode. The positive transition altitude comparative results are shown in Figs.15, 22, and the reverse transition altitude comparative results are shown in Figs.19, 25. It can be seen that the altitude results in Strategy Ⅰ are smoother than those in Strategy Ⅱ. The forward speed results in Strategy Ⅰ are also smoother than those in Strategy Ⅱ (Figs.16, 23 (positive transition), and Figs.20, 26 (reverse transition)).

In Strategy Ⅱ, the positive transition is completed without an initial forward flight speed. The deficiency of Strategy Ⅱ is an instantaneous switch between the multirotor control and the fixed-wing control, which causes altitude variation at the moment of switching. In addition, the values of the rotor tilting angle and the forward flight speed are all increased in the positive transition, which indicates that if the changing rate of the rotor tilting angle is large, and the forward flight speed is smaller than that at the level flight, the aerodynamic control surfaces could be incapable to control the UAV. In this case, the hover mode should be switched immediately and the multirotor control is used to achieve a stable flight.

4 Conclusions

This paper studies the altitude control of a tilt tri-rotor UAV in the transition mode. A GWO-based RBFNN control scheme is proposed to achieve the altitude control and the attitude control for the tilt tri-rotor UAV under different disturbances. The tracking signals of the reference command are obtained by adopting TD, and the parameters of RBFNN controllers are obtained by GWO. Numerical simulation results show that the proposed method control results are better than those by ADRC and PID, which are reflected by the maximum tracking error and the steady-state error. Even under disturbances, the stable altitude control performance in the transition mode can be achieved, which demonstrates the robustness of the proposed method and the effectiveness of the proposed altitude control strategies. The future work will focus on implementing the proposed method to real flights.

References

[1] CARDOSO D N, ESTEBAN S, RAFFO G V. A new robust adaptive mixing control for trajectory tracking with improved forward flight of a tilt-rotor UAV[J]. ISA Transactions, 2021, 110: 86-104.

[2] YANG Yang, CHEN Weiqin, CHEN Renliang. Design of redundant manipulation for quad tilt rotor aircraft[J]. Journal of Nanjing University of Aeronautics & Astronautics, 2020, 52(2): 255-263. (in Chinese)

[3] XUE Meng, SUN Qiang. Tiltrotor military requirement and critical technology analysis[J]. Helicopter Technique, 2020(1): 47-49. (in Chinese)

[4] WANG Zhigang, DUAN Dengyan, YANG Yongwen, et al. Analysis of flight dynamics characteristics of tilt quad rotor with partial tilt-wing[J]. Transactions of Nanjing University of Aeronautics and Astronautics, 2019, 36(6): 938-951.

[5] LI Peng, ZHAO Qijun, WANG Zhengzhong, et al. Highly-efficient CFD method for predicting aerodynamic force of tiltrotor in conversion mode[J]. Journal of Nanjing University of Aeronautics & Astronautics,

2015, 47(2): 189-197. (in Chinese)

[6] LU Taoye, CHEN Renliang, ZENG Lifang, et al. Mathematical model for performance of coaxial tilt-rotor[J]. Journal of Nanjing University of Aeronautics & Astronautics, 2017, 49(3): 396-402. (in Chinese)

[7] DU Siliang, WANG Ce, SUN Hongjia, et al. Numerical analysis of aerodynamic interference of rotor/fuselage in transition state of tilting four-rotor UAV[J]. Journal of Nanjing University of Aeronautics & Astronautics, 2018, 50(2): 179-185. (in Chinese)

[8] GOVDELI Y, MUZAFFAR S M B, RAJ R, et al. Unsteady aerodynamic modeling and control of pusher and tilt-rotor quadplane configurations[J]. Aerospace Science and Technology, 2019, 94: 105421.

[9] CHIAPPINELLI R, COHEN M, DOFF-SOTTA M, et al. Modeling and control of a passively-coupled tilt-rotor vertical takeoff and landing aircraft[C]//Proceedings of 2019 International Conference on Robotics and Automation. Montreal, QC, Canada: IEEE Press, 2019: 4141-4147.

[10] HUO Yujia, LI Yiping, FENG Xisheng. Tiltrotors position tracking controller design using deep reinforcement learning[C]//Proceedings of 2019 5th International Conference on Mechanical and Aeronautical Engineering. Sanya, China: IOP Conference Series: Materials Science and Engineering, 2020, 751: 012047.

[11] LIU Ningjun, CAI Zhihao, ZHAO Jiang, et al. Predictor-based model reference adaptive roll and yaw control of a quad-tiltrotor UAV[J]. Chinese Journal of Aeronautics, 2020, 33(1): 282-295.

[12] YANG Jie, CHEN Mou, XIONG Shixun, et al. Average dwell time switching robust H_∞ tracking control for a tiltrotor aircraft[J]. Control Theory & Applications, 2020, 37(5): 1018-1027. (in Chinese)

[13] WANG Zhigang, LI Jianbo. A novel active disturbance rejection control for the quad tilt rotor in conversion process[J]. IOP Conference Series: Earth and Environmental Science, 2020, 440: 032036.

[14] WANG Zhigang, ZHAO Hong, DUAN Dengyan, et al. Application of improved active disturbance rejection control algorithm in tilt quad rotor[J]. Chinese Journal of Aeronautics, 2020, 33(6): 1625-1641.

[15] YU Li, HE Guang, ZHAO Shulong, et al. Dynamic inversion-based sliding mode control of a tilt tri-rotor UAV[C]//Proceedings of 2019 12th Asian Control Conference. Kitakyushu, Japan: IEEE Press, 2019: 1637-1642.

[16] WU Wenhai, WANG Jie, LIU Jintao, et al. Carrier landing robust control based on longitudinal decoupling[J]. Transactions of Nanjing University of Aeronautics and Astronautics, 2017, 34(6): 609-616.

[17] WANG Ruonan, JIANG Bin, LIU Jianwei. Fault estimation and accommodation for a class of nonlinear system based on neural network observer[J]. Transactions of Nanjing University of Aeronautics and Astronautics, 2018, 35(2): 318-325.

[18] PAN Muxuan, HUANG Jinquan. Model reference adaptive control based on nonlinear compensation for turbofan engine[J]. Transactions of Nanjing University of Aeronautics and Astronautics, 2012, 29(3): 215-221.

[19] CHEN Qi, JIANG Tao, SHI Fengming, et al. Longitudinal attitude control for a tilt tri-rotor UAV in transition mode[J]. Flight Dynamics, 2016, 34(6): 49-53. (in Chinese)

[20] DREIER M E. Introduction to helicopter and tiltrotor flight simulation[M]. Beijing: Aviation Industry Press, 2014: 123-252. (in Chinese)

[21] LIU Ningjun. Study on efficient flight mode transition control of V/STOL UAV[D]. Beijing: Beihang University, 2019. (in Chinese)

[22] CHEN Chao. Research on control method for the transition mode of the small tilt-rotor UAV[D]. Changsha: National University of Defense Technology, 2019. (in Chinese)

[23] WU Sentang. Flight control system[M]. 2nd ed. Beijing: Beihang University Press, 2013: 8-60. (in Chinese)

[24] LIU Jinkun. RBF neural network control for mechanical systems: Design, analysis and MATLAB simulation[M]. 2nd ed. Beijing: Tsinghua University Press, 2014: 57-60. (in Chinese)

[25] MIRJALILI S, MIRJALILI S M, LEWIS A. Grey wolf optimizer[J]. Advances in Engineering Software, 2014, 69(3): 46-61.

[26] PRECUP R E, DAVID R C, SZEDLAK-STINEAN A I, et al. An easily understandable grey wolf optimizer and its application to fuzzy controller tuning[J]. Algorithms, 2017. DOI:10.3390/a10020068.

[27] LIU Yuan, HUANG Xianghua, SUN Qingbiao, et al. Integrated optimization control of performance and jet noise of turbofan engine based on improved grey wolf optimization algorithm[J]. Journal of Nanjing University of Aeronautics & Astronautics, 2020, 52(4): 532-539. (in Chinese)

[28] BAI Yuan, CHEN Jingrong, ZHAN Zhichan. Analysis and research of improved grey wolf optimization al-

gorithm[J]. Computer Science and Application, 2017, 7(6): 562-571.

[29] YU Yue, WANG Honglun, LI Na, et al. Automatic carrier landing system based on active disturbance rejection control with a novel parameters optimizer[J]. Aerospace Science and Technology, 2017, 69: 149-160.

[30] ZHANG Fei, LU Ping, JIANG Tao, et al. Transitional mode manipulation strategy of tilt tri-rotor UAVs based on fuzzy control[J]. Electronics Optics & Control, 2018, 25(4): 32-36. (in Chinese)

[31] TA D A, FANTONI I, LOZANO R. Modeling and control of a tilt tri-rotor airplane[C]//Proceedings of 2012 American Control Conference. Montreal, QC, Canada: IEEE Press, 2012: 131-136.

Authors Mr.**MA Yan** is a Ph.D. candidate in Beihang University. His research focuses on tilt rotor UAV flight control. Prof. **WANG Yingxun** is a doctoral supervisor in Beihang University. His research focuses on autonomous control of UAVs.

Author contributions Mr. **MA Yan** complied the models, performed the figure generation, and wrote the manuscript. Prof. **WANG Yingxun** designed the study, conducted the analysis, and interpreted the results. Prof. **CAI Zhihao** designed the study, conducted the analysis, and interpreted the results. Prof. **ZHAO Jiang** designed the study, conducted the analysis, and interpreted the results. Dr. **LIU Ningjun** complied the models. All authors commented on the manuscript draft and approved the submission.

Competing interests The authors declare no competing interests.

(Production Editor: XU Chengting)

倾转三旋翼无人机倾转定高控制研究

马 延[1], 王英勋[1,2], 蔡志浩[1], 赵 江[1], 刘宁君[2]

(1.北京航空航天大学自动化科学与电气工程学院, 北京 100083,中国; 2.北京航空航天大学无人系统研究院, 北京 100083,中国)

摘要:针对倾转旋翼无人机在倾转过程中的高度控制问题,提出一种基于灰狼优化的神经网络自适应控制方法,用于一种倾转三旋翼无人机倾转过程的飞行控制。首先,建立了无人机的非线性数字仿真模型;其次,基于神经网络自适应控制方法分别设计了无人机的高度控制器和姿态控制器,并用灰狼优化算法对神经网络的参数和控制器的参数寻优;再次,设计了倾转过程中的两种高度控制方案;最后,通过数字仿真验证了本文所提出的控制方法的有效性和鲁棒性。

关键词:倾转三旋翼无人机;高度控制;神经网络自适应控制;灰狼优化算法